Full-scale chemical and field-effect passivation: 21.52% efficiency of stable MAPbI₃ solar cells via benzenamine modification

Fengyou Wang[1,2,3], Meifang Yang[1,3], Yuhong Zhang[1,3], Jinyue Du[1,3], Shuo Yang[4], Lili Yang[1,2,3] (✉), Lin Fan[1,2,3], Yingrui Sui[1,2,3], Yunfei Sun[1], and Jinghai Yang[1,2,3] (✉)

[1] Key Laboratory of Functional Materials Physics and Chemistry of the Ministry of Education, Jilin Normal University, Changchun 130103, China
[2] National Demonstration Center for Experimental Physics Education, Jilin Normal University, Siping 136000, China
[3] Key Laboratory of Preparation and Application of Environmental Friendly Materials, Ministry of Education, Jilin Normal University, Changchun 130103, China
[4] College of Science, Changchun University, Changchun 130022, China

ABSTRACT

Organic-inorganic metal halide perovskite solar cells have achieved high efficiency of 25.5%. Finding an effective means to suppress the formation of traps and correlate stability losses are thought to be a promising route for further increasing the photovoltaic performance and commercialization potential of perovskite photovoltaic devices. Herein, we report a facile passivation model, which uses a multi-functional organic molecule to simultaneously realize the chemical passivation and field-effect passivation for the perovskite film by an upgraded anti-solvent coating method, which reduces the trap states density of the perovskite, improves interface charge transfer, and thus promotes device performance. In addition, the hydrophobic groups of the molecules can form a moisture-repelling barrier on the perovskite grains, which apparently promotes the humidity stability of the solar cells. Therefore, the optimal power conversion efficiency (PCE) of perovskite solar cells after synergistic passivation reaches 21.52%, and it can still retain 95% of the original PCE when stored in ~ 40% humidity for 30 days. Our findings extend the scope for traps passivation to further promote both the photovoltaic performance and the stability of the perovskite solar cells.

KEYWORDS

chemical passivation, anti-solvent, MAPbI₃ solar cells, recombination, charge transfer

1 Introduction

Hybrid organic-inorganic perovskite solar cells (PSCs) are becoming a spotlight owing to their low-cost and high power conversion efficiencies (PCEs) for massive production [1–4]. A PCE of 25.5% has been reported by now [5], which is comparable to the commercialized silicon solar cells and become the auspicious photovoltaic devices. However, the defects on the surface and grain boundaries (GBs) of the as-prepared polycrystalline perovskite films are ready to be the site of non-radiative recombination for photo-excited charges [6–9]. The recombination limits the diffusion of carriers [10], reduces the minority carrier lifetime, and causes the ions migration and diffusion [11, 12], which in turn declines the PCEs and stability of PSCs. Hence, suppressing the non-radiative recombination at the perovskite surface and GBs is essential for achieving a high-performance and stable PSCs [13–15].

Currently, interface engineering and additive engineering are mainstream techniques for eliminating the defect states of the perovskite surface and enlarging the crystal size of perovskite to reduce recombination [14–19]. For example, the semiconductor molecule fullerene has been verified its advantages for passivating the trap states at GBs within the perovskite film. Because of the formation of fullerene-halide radicals, the Pb-I

translocation defects within the perovskite films have been virtually eliminated [20–22]. Also, Huang et al. and Sargent et al. [23, 24] have inserted different types of insulting polymers as the ultrathin passivation layer into the perovskite/electron transport layer (ETL) hetero-interface to passivate the interfacial defects, thereby reduced the interfacial recombination losses and improved the device performance. White et al. [25, 26] adopted an ultrathin passivation layer consisting of poly(methyl methacrylate) and fullerene derivative mixture to passivate defects at the perovskite/TiO₂ interface, significantly suppressing interfacial recombination; then, they reported a novel two-dimensional (2D)/three-dimensional (3D) PSCs using a mixed cation composition of 2D perovskite based on two different isomers of butylammonium iodide, enabling an high efficiency of 23.27%. You et al. [27] reported the using of an organic halide salt phenethylammonium iodide (PEAI) on perovskite films for surface passivation, which enables a high certificated efficiency of 23.32%. Previously, we have proposed an iodine-assisted upgraded anti-solvent strategy to control the crystallization and passivate the traps of perovskite, which also improves the PCE and long-term stability of solar cells [4]. The ultimate goal of these strategies can be summed up as "chemical passivation (CP)", which is intentionally constructing chemical bond (hydrogen bond, ionic bond, coordination bond, etc.) between

---

perovskite traps and the external active agents, thus reducing the photo-excited charge recombination. While the molecular for CP must be exquisitely designed to eliminate the extra series resistance and charge transfer barrier, otherwise it will degrade the performance of the devices.

In retrospect, field-effect passivation (FEP), which has been successfully implemented on silicon solar cells, is another ingenious passivation strategy [28–32]. It establishes strong interfacial dipoles by covering a dielectric film on photo-absorber surface, which aims to selectively repel one charge (electron/hole) and attract another charge (hole/electron). That is to say, the FEP can decline the probability of photo-excited electron/hole recombination even without forming an extra chemical bond, thereby alleviating interface recombination and enhancing charge transfer. Accordingly, it is meaningful and crucial to developing the suitable passivation materials that can simultaneously provide the function of CP and FEP on PSCs, and revealing the corresponding operation mechanism in details.

For PSCs application, the ideal passivation materials that can achieve both FEP and CP should have appropriate chemical ligands to terminate the traps and a fixed majority carrier concentration to form the interface dipoles. In line with these requirements and our previous experiences, we found that a small semiconductor molecule, 4,4-cyclohexylidenebis[N,N-bis(4-methylphenyl)benzenamine] (TAPC) may be a potential alternative to achieve full-scale passivation for PSCs. The lone pair electrons of N atom in TAPC could chemically passivate Pb^{2+} defects within the perovskite film. Also, Yu et al. and Yang et al. [33, 34] reported that TAPC as archetypical p-type materials can provide FEP in silicon solar cells, which is beneficial to reducing interface recombination and boost charge transfer.

Based on the above research background, we proposed a universal and straightforward approach to introduce the TAPC into MAPbI$_3$ through a one-step anti-solvent method. This method judiciously combines the application of CP and FEP in the perovskite film, hence successfully reducing the interface recombination loss and enhancing the hole extraction. As an additional benefit, we found the –CH$_3$ tails of TAPC can form a moisture-repelling barrier on the MAPbI$_3$ grains, thereby improving the stability of the device in a humid environment. The operation mechanism of charge transfers kinetic, interfacial passivation, and device performance has been interpreted in detail.

Ultimately, a high PCE of 21.52% in mesoscopic n-i-p MAPbI$_3$ solar cells is achieved. In room temperature, the cells degrade only ~ 5% after 30 days of exposure in 40% relative humidity.

## 2 Experimental section

Fabrication of MAPbI$_3$: 163 mg of MAI and 462 mg of PbI$_2$ were mixed in solvent of dimethylformamide (DMF) and dimethyl sulfoxide (DMSO) (v:v = 7:3) as the perovskite precursor. 5.5 mg of TAPC was dissolved in the 1 mL chlorobenzene (CB) solution as an upgraded anti-solvent. The precursor solution of perovskite was spin-coated onto the mesoporous TiO$_2$ layer at 4,000 rpm. During this process, 300 μL CB or upgraded anti-solvent was dripped at the beginning 30 s. Then, the obtained film was annealed at 60 °C for 5 min and 100 °C for 10 min to form the perovskite film. The entire perovskite film is prepared in a nitrogen glove box.

The detailed information regarding to the materials, the preparation of PSCs, and the corresponding characterization were provided in the Electronic Supplementary Material (ESM) as Supplementary Notes 1, 2 and 3, respectively.

3 Results and discussion

First, we studied the molecular structure and film properties of TAPC. TAPC is constructed by two tri(p-tolyl) amine (TTA) molecules chemically bridged by a cyclohexane ring (Fig. 1(a)) [35]. The molecular surface potential diagram of TAPC has obvious densely distributed areas of electron clouds (Fig. 1(b)), which are potential sites that can provide electrons. In addition, the –CH$_3$ group of the TAPC enables the molecule to be hydrophobic, which can be confirmed the water contact angle test (Fig. 1(c)). Figure S1 in the ESM shows the absorption and PL spectrum of TAPC film. The PL spectrum shows noticeable shoulders in the asymmetric 500 nm center band, which is due to the different configurations of adjacent molecular species that form excimers on crystal defects [36]. Figure S2 in the ESM shows the Fourier transform infrared (FTIR) spectrum of TAPC powder. Consistent with previous reports, the absorption bands at 1,505, 1,602, and 2,937 cm^{-1} are ascribed to the C–N stretch, the para-aromatic ring stretch, and N–H stretch, respectively [37, 38]. The peaks at 3,000–3,200 cm^{-1} come from the aromatic C–H stretch. The abundant chemical bonds
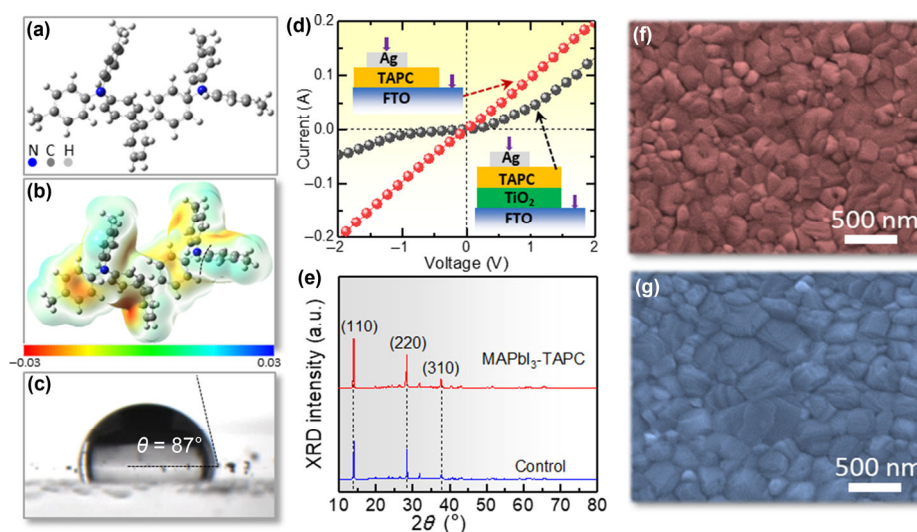

Figure 1 Analyze the properties of TAPC and demonstrating the enhancement of perovskite crystallization caused by TAPC. (a) The molecular structure of TAPC. (b) The molecular surface potential of TAPC. (c) The water contact angle test of TAPC film. (d) The *I–V* characters of the devices with a structure of Ag/TAPC/FTO (red) and Ag/TAPC/TiO$_2$/FTO (black), respectively. (e) XRD intensity of the control and MAPbI$_3$-TAPC films. SEM images of (f) control and (g) MAPbI$_3$-TAPC films.

provide variety of choices for passivating perovskite. We used the current-voltage (*I–V*) test with a setup of Ag/TAPC/FTO and Ag/TAPC/TiO₂/FTO to evaluate the electrical performance of TAPC (Fig. 1(d)). Compared with the *I–V* curve of the single TAPC layer, the *I–V* curve of the TAPC/TiO₂ shows obvious rectification character, which proves the p-type nature of TAPC layer. In this study, we dissolved TAPC in CB as an upgraded anti-solvent for preparing the MAPbI₃ films. The X-ray diffraction (XRD) and scanning electron microscope (SEM) were performed to investigate the influence of TAPC on the morphology and crystal structure of the MAPbI₃ films. The XRD patterns of the perovskite films before and after the TAPC treatment are shown in Fig. 1(e). Two typical major diffraction peaks at ~ 14.4° and 28.8° could be indexed as (110) and (220) crystal plane of the MAPbI₃, which is agreed with previously report [39]. However, the TAPC-treated MAPbI₃ film (MAPbI₃-TAPC) demonstrates stronger reflective diffraction intensity than the control film (Table S1 in the ESM), indicating a better crystallinity. Moreover, the (110)/(310) peak ratio was improved from 5.71 to 8.13 after TAPC treatment, implying the TAPC treatment improved the preferred orientation of the perovskite films. The SEM images (Figs. 1(f) and 1(g)) also show that the crystal size of the MAPbI₃-TAPC film is larger and more uniform than that of the control film (the reason will be revealed in the following context). The size distribution of the control film and the MAPbI₃-TAPC film is shown in Fig. S3 in the ESM. One can see that the grains size of MAPbI₃-TAPC film is ~ 100 nm larger than that of the control film. The MAPbI₃-TAPC film also has stronger light absorption than the control film due to the improved crystallization, which can be observed from the images and absorbance spectra in Fig. S4 in the ESM.

Generally, good surface morphology and crystallinity of the film will reduce the grain boundary density where most defects are located. We further used the time-resolved photoluminescence

(TRPL) spectroscopy to detect the non-radiative recombination within the perovskite films (Fig. 2(a) and Table S2 in the ESM). For the Glass/sample (control or MAPbI₃-TAPC) setup, the MAPbI₃-TAPC film exhibits a longer decay time, which indicates the traps-induced non-radiative recombination has been suppressed by the passivation of TAPC. Furthermore, the space-charge-limited-current (SCLC) test on a hole-only device with an architecture of FTO/PEDOT: PSS/perovskite/ spiro-OMeTAD/Ag was taken to study the trap density (N_{trap}) of the perovskite film (Fig. 2(b)). The device structure diagram and the calculation of N_{trap} are demonstrated in (Fig. S5 in the ESM). The N_{trap} of the MAPbI₃-TAPC was 3.18×10^{15} cm⁻³, which is lower than that of the control film (1.04×10^{16} cm⁻³). In addition, Urbach absorption has also been performed to detect the band-tail states of the perovskite films, which is considered as a valuable parameter indicating the effects of all possible defects [40]. As shown in Fig. 2(c), the Urbach energy (E_u) value of MAPbI₃-TAPC film (29.34 meV) is lower than that of the control film (54.17 meV), which also indicates that the N_{trap} of MAPbI₃-TAPC film is reduced. The FTIR as well as the X-ray photoelectron spectroscopy (XPS) was performed to reveal the passivation details. The FTIR spectroscopy shows that the N–H bend of perovskite redshift from 1,464 to 1,468 cm⁻¹, and the N–H bond strength redshift from 3,102 to 3,116 cm⁻¹ (Fig. 2(d) and Fig. S6 in the ESM). Moreover, compared with the control film, the XPS patterns of both Pb 4f and I 3d core signals of MAPbI₃-TAPC shift slightly towards the lower binding energies (Figs. 2(e) and 2(f)). Some researchers have proposed that the interaction between passivation agents and perovskite could change the bond vibration and Pb 4f binding energy of the perovskite [41–44]. Therefore, as depicted in Fig. 2(g), the reduction of trap states in the MAPbI₃-TAPC film can be ascribed to the interaction between the MAPbI₃ and TAPC, which mainly occurs via passivates the Pb²⁺ dangling bonds by the N of TAPC (Fig. 2(g)) [6]. In addition, due to the interaction
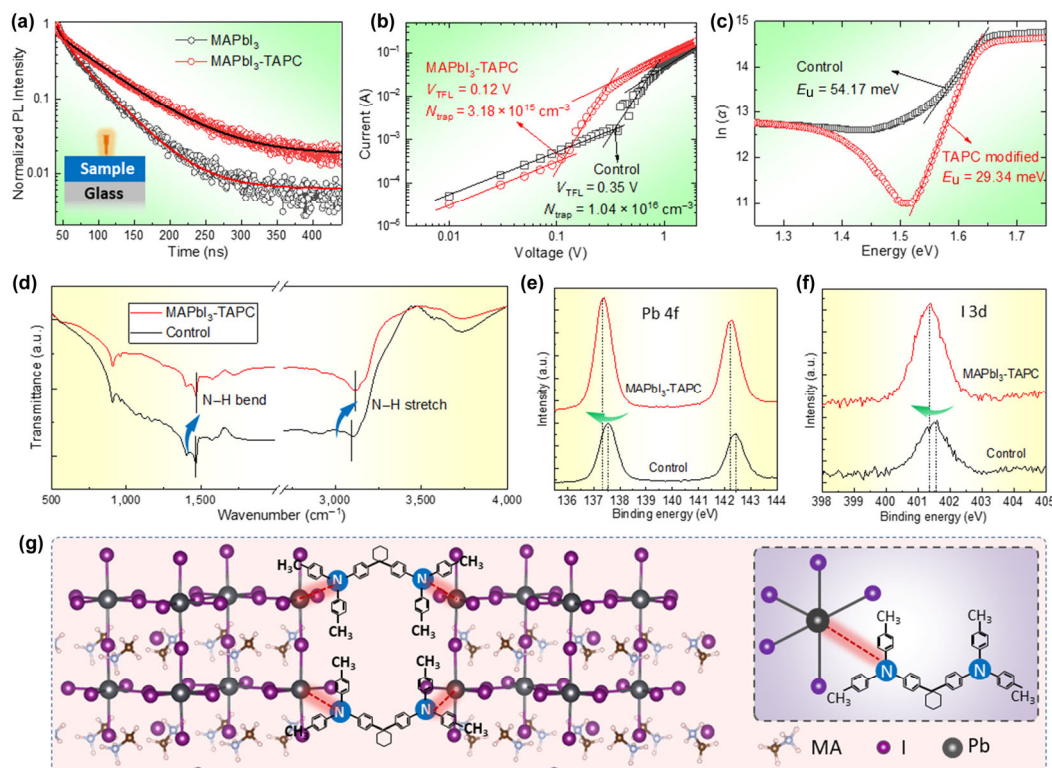
Figure 2 CP-induced trap states elimination in MAPbI₃ film. (a) The TRPL spectra for the control and MAPbI₃-TAPC films, respectively. (b) The SCLC curves and (c) E_u value of the corresponding sample. (d) FTIR spectrum of the corresponding sample; XPS core level peaks of Pb 4f and I 3d of the (e) MAPbI₃ and (f) MAPbI₃-TAPC. (g) Schematic diagram of chemical passivation induced by TAPC incorporation.

between TAPC and Pb^{2+}, the crystallization process is inevitably retarded, which is similar to previous findings [41, 42]. The slow crystallization process is conducive to enlarging the grain size and can be observed in Figs. 1(f) and 1(g).

In addition to chemical passivation, TAPC as an archetypical p-type molecule has a certain impact on the interfacial electric field, which in turn affects the charge transport. As shown in Fig. S7 in the ESM, TAPC has a bandgap of 3.5 eV and a Fermi level of 5.1 eV. Compared with the of $MAPbI_3$ (work function ~ 4.6 eV), the work function difference between $MAPbI_3$ and TAPC will inevitably cause the charge migration, resulting in interfacial dipoles (Fig. 3(a)). Similarly, we have observed this phenomenon at MoO_x/Si interface [45, 46]. This interfacial polarization can efficiently separate photo-generated carriers and reduce the probability of Shockley-Read-Hall (SRH) recombination [47], thus act as an FEP in PSCs. To visualize the origination of FEP on the perovskite film, we used scanning Kelvin probe microscopy (SKPM) to show the surface potential change. The experimental setup is demonstrated in Fig. 3(b). The results show that a ~ 55 mV of positive surface potential is changed when the probe is sweeping from the control film to the $MAPbI_3$-TAPC film (Figs. 3(c) and 3(d)). In addition, the surface potential of $MAPbI_3$-TAPC film is more uniform than that of the control film (Fig. S8 in the ESM). As reported by Cao et al. [48], this phenomenon means a microscopic electric dipole moment with the positive charge end pointing toward the active layer (perovskite film) and the negative charge end pointing toward the modification layer (TAPC), which is conducive to extracting holes and repelling electrons (Fig. 3(a)) [49]. In order to further confirm the enhanced interfacial charge transport at $MAPbI_3$-TAPC/Spiro-OMeTAD interface, we conducted another TRPL test (Fig. 3(d)). The decay based on Glass/$MAPbI_3$-TAPC/HTL is faster than that of Glass/control/HTL, which indicates that the TAPC interlayer promotes hole extraction. Furthermore, through the C^{-2}–V curve, we found that the Fermi level difference (V_{bi}) of the $MAPbI_3$-TAPC device is 1.08 V, which is indeed higher than that of the control device (0.99 V) (Fig. 3(e)). The enhanced V_{bi} is beneficial to efficiently collect holes and repel electrons at the hetero-interface, thereby reducing the interfacial recombination and enhancing the photovoltaic performance. These results demonstrate that the TAPC can not only reduces the traps states of $MAPbI_3$ films by CP, but also improves the interface charge transfer through FEP, which is expected to improve the overall performance of the PSCs.

We further fabricated the n-i-p PSCs (FTO/m-TiO_2/perovskite/Spiro-OMeTAD/Ag), as shown in Figs. 4(a) and 4(b). Figure 4(c) shows the J–V curves of the champion PSCs measured under both forward and reverse scan. The output parameters of the PSCs are shown in Table 1. The PCE of the control device obtained from the forward- and reverse-scan were 17.95% and 19.62% respectively, which is a typical PCE for $MAPbI_3$ solar cells. Consistent with the previous reports [50], the control device shows clear hysteresis due to the recombination-induced interfacial capacitance effect. For the $MAPbI_3$-TAPC devices, we have optimized the TAPC concentration and found that the 5.5 mg/mL is suitable for PSCs application (Fig. S9 in the ESM). For the champion $MAPbI_3$-TAPC cell, the reverse scan of FF is 80.26%, V_{oc} is 1.17 V, J_{sc} is 22.92 mA·cm^{-2}, and overall PCE is 21.52%. The PCE for forward scan is 21.08% (FF = 79.74%, V_{oc} = 1.16 V, J_{sc} = 22.79 mA·cm^{-2}). The reduced J–V hysteresis and improved PCE can be ascribed to the synergy of CP and FEP, which simultaneously reduces the interface recombination and enhances the carrier transport. Figure 4(d) exhibits the external quantum efficiency (EQE) spectra of the PSCs. The $MAPbI_3$-TAPC device shows a higher spectrum response in the long wavelength region than the control device. We further characterized open-circuit photovoltage decay (OCVD) of the devices to confirm the enhanced performance of the devices [51]. As shown in Fig. 4(e), the OCVD time of the $MAPbI_3$-TAPC device is longer than that of the control device, suggesting that the recombination losses within $MAPbI_3$-TAPC device are suppressed. This result is in line with the enhanced V_{oc} in the $MAPbI_3$-TAPC devices. The electrochemical impedance spectroscopy (EIS) measurements were used to further elucidate the internal electrical properties of the PSCs. The Nyquist plot with the frequency range of 100 Hz to 1 MHz measured is shown in Fig. 4(f) and Table S3 in the ESM. We found a marked drop in charge transfer recombination resistance (R_{tr}) and an increase in recombination resistance (R_{rec}), which suggests an enhanced interface contact and suppressed charge recombination after incorporating the TAPC interlayer.

Except for the photovoltaic performance enhancement, since the –CH_3 of TAPC is a hydrophobic group, the contact angle of water of the $MAPbI_3$-TAPC film is increased (Figs. 5(a) and 5(b)), which is conducive to improving the stability of the PSCs [52–55]. This can be verified by the XRD patterns of the perovskite films after aging for 30 days (Fig. 5(c)). The control film shows a slight PbI_2 peak at 12.4° after aging, while the $MAPbI_3$-TAPC film still keeps a well-maintained crystal structure without observable PbI_2 peak. We further evaluated the repeatability and long-term stability of the solar cells. The statistical distribution of efficiency based on 50 devices suggested the reliability and repeatability of the $MAPbI_3$-TAPC devices are better than that of the control devices (Fig. 5(d)). The steady-state PCE with a bias voltage at the maximum power point (V_{mpp}) was measured to confirm the operation output. As shown in Fig. 5(e), the steady-state PCE of the champion
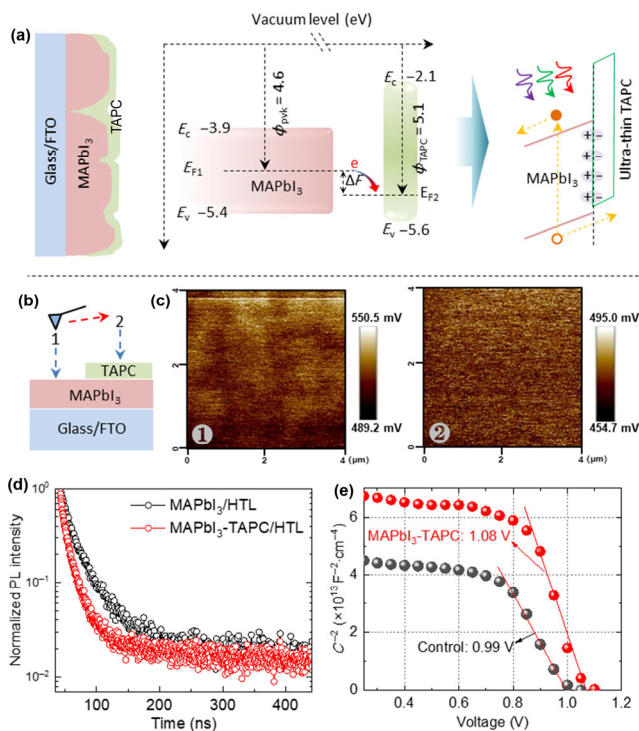
Figure 3 TAPC-induced FEP improves charge transfer at the hetero-interface. (a) Schematic diagram of interface polarization formed by TAPC passivation. (b) The setup for SKPM measurement. (c) The SKPM images of the sample. Region 1: The active layer ($MAPbI_3$). Region 2: The TAPC covered $MAPbI_3$. (d) The TRPL spectra and (e) C^{-2}–V curves of the corresponding devices.
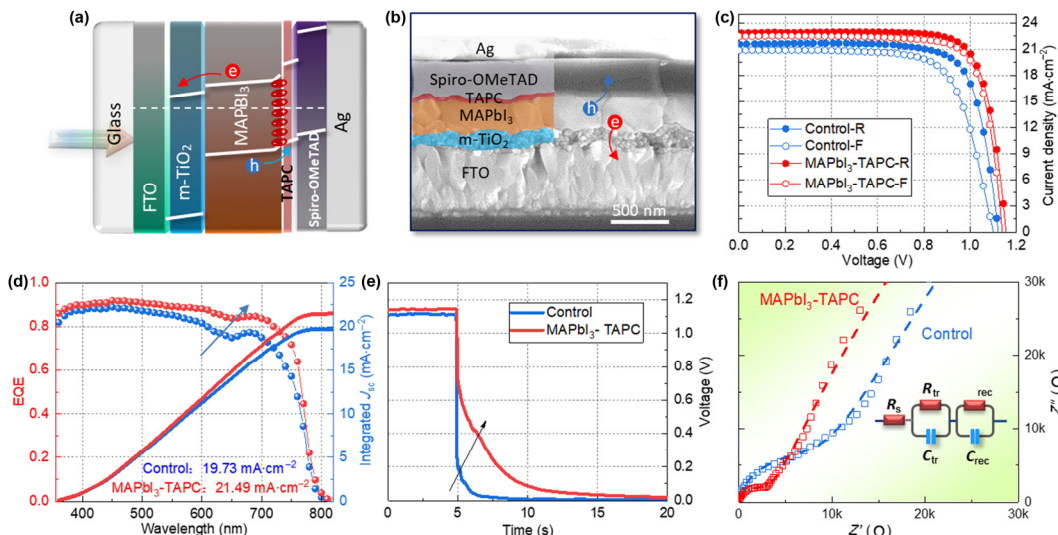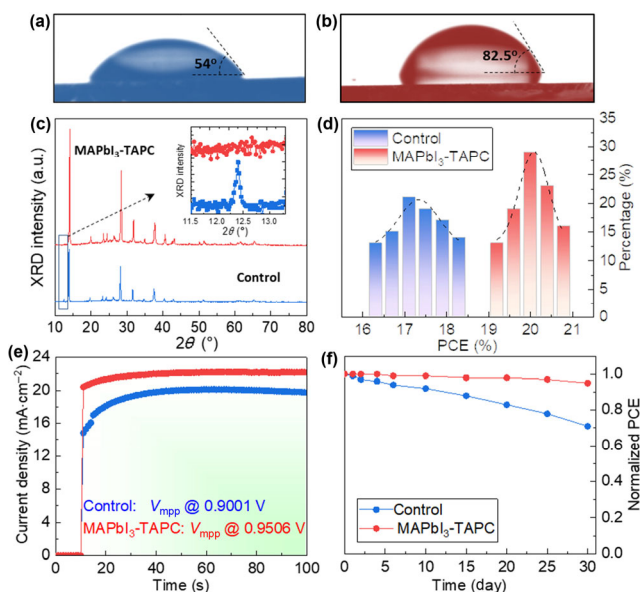
Figure 4 Device performance. (a) The schematic structure and (b) the cross-section of the device. (c) The illuminated *J*–*V* curves of the PSCs under forward- and reverse-scan, respectively. (d) The EQE, (e) OCVD, and (f) Nyquist plot of PSCs. The hollow square and dash line in (f) is the test data and the fitted data, respectively.

Table 1 The output parameters of the PSCs based on control and MAPbI$_3$-TAPC under different scanning direction

Device		J_{sc} (mA·cm^{-2})	V_{oc} (V)	FF (%)	PCE (%)
Control	R–S	22.18	1.15	76.91	19.62
	F–S	21.56	1.13	73.68	17.95
MAPbI$_3$-TAPC	R–S	22.92	1.17	80.26	21.52
	F–S	22.79	1.16	79.74	21.08

Figure 5 Stability of the devices. The water contact angle of (a) the control and (b) the MAPbI$_3$-TAPC films. (c) The XRD patterns of the control and MAPbI$_3$-TAPC films. (d) The PCEs distribution collected from 50 PSCs. (e) The output photocurrent extracted from the V_{mpp} bias of corresponding devices. (f) The normalized PCEs decay of the PSCs based on control and MAPbI$_3$-TAPC samples.

devices based on control and MAPbI$_3$-TAPC films are 18.09% and 21.10%, respectively. Figure 5(f) shows the normalized PCE against periodical time. As expected, the MAPbI$_3$-TAPC PSCs show enhanced ambient stability compare to the control ones. Exposing the PSCs under the environment with 40% humidity for 30-days, the MAPbI$_3$-TAPC device retained 95%

of the initial PCE. We have studied the operational stability of the PSCs under MPP tracking with continuous light irradiation a N$_2$ atmosphere (Fig. S10 in the ESM). The control cell (MAPbI$_3$) shows a rapid loss of PCE (down to 81% of the initial PCE after irradiated 100 h), and the MAPbI$_3$-TAPC cell presents a better long-term stability, keeping more than 92% of original PCE after 100 h irradiation. This further verifies that the full-scale passivation brought by incorporating TAPC remarkably enhances the long-term stability of the PSCs.

4 Conclusions and perspectives

In conclusion, the photovoltaic performance of PSCs has been promoted by processing perovskite films with multi-functional organic molecule to simultaneously achieve the CP and FEP. It was proved that in the PSCs with n-i-p structure, the concerted passivation induced by TAPC molecules onto the perovskite film can both passivate the trap states and effectively extract holes. In contrast to the control device, the PCE of the MAPbI$_3$-TAPC device enhanced from 19.62% to 21.52%, and stability was significantly improved. In addition, the –CH$_3$ groups of TAPC molecule forms a moisture-repelling barrier on the MAPbI$_3$ particles, which significantly enhances the humidity stability of the film. The MAPbI$_3$-TAPC device keeps 95% of the initial PCE when stored for 30 days under 40% humidity. For the long-term perspective, it demonstrates that TAPC molecules can be a multifunctional alternative for passivating the perovskite. To further promote the photovoltaic performance of PSCs, we should take care of the FEP at the opposite ETL/perovskite interface by incorporating low work function interlayer, which can form bifacial FEP in PSCs. Ultimately, considering the recombination dynamic and defects-induced ion migration, we believe that the passivation of defects and effective charge extraction at the interface are key factors for further high performance and stable PSCs. For the foreseeable future, combining CP and FEP will synchronously terminate the active traps and enhance the interface charge transfer, hence triggering another routine for boosting the photovoltaic performance of the device.

Electronic Supplementary Material: Supplementary material (FTIR and UV–vis absorption of the TAPC; UV–vis absorption, FTIR, XPS, UPS and SKPM of the MAPbI$_3$; SCLC measurement; performance of the solar cells; and detailed fabrication process; the fitted parameters of the TRPL curve) is available in the online version of this article at https://doi.org/10.1007/s12274-020-3286-2.

References

[1] Xing, G. C.; Mathews, N.; Sun, S. Y.; Lim, S. S.; Lam, Y. M.; Grätzel, M.; Mhaisalkar, S.; Sum, T. C. Long-range balanced electron- and hole-transport lengths in organic-inorganic CH$_3$NH$_3$PbI$_3$. *Science* **2013**, *342*, 344–347.

[2] Kang, C. H.; Dursun, I.; Liu, G. Y.; Sinatra, L.; Sun, X. B.; Kong, M. W.; Pan, J.; Maity, P.; Ooi, E. N.; Ng, T. K. et al. High-speed colour-converting photodetector with all-inorganic CsPbBr$_3$ perovskite nanocrystals for ultraviolet light communication. *Light Sci. Appl.* **2019**, *8*, 94.

[3] Yan, L. L.; Han, C.; Shi, B.; Zhao, Y.; Zhang, X. D. A review on the crystalline silicon bottom cell for monolithic perovskite/silicon tandem solar cells. *Mater. Today Nano* **2019**, *7*, 100045.

[4] Wang, F. Y.; Yang, M. F.; Yang, S.; Qu, X.; Yang, L. L.; Fan, L.; Yang, J. H.; Rosei, F. Iodine-assisted antisolvent engineering for stable perovskite solar cells with efficiency >21.3%. *Nano Energy* **2020**, *67*, 104224.

[5] Best Research-Cell Efficiencies[Online]. NREL, https://www.nrel.gov/pv/assets/pdfs/cell-pv-eff-emergingpv.20200919.pdf (accessed 25 September 2020).

[6] Wu, W. Q.; Yang, Z. B.; Rudd, P. N.; Shao, Y. C.; Dai, X. Z.; Wei, H. T.; Zhao, J. J.; Fang, Y. J.; Wang, Q.; Liu, Y. et al. Bilateral alkylamine for suppressing charge recombination and improving stability in blade-coated perovskite solar cells. *Sci. Adv.* **2019**, *5*, eaav8925.

[7] Huang, D.; Goh, T.; Zheng, Y. F.; Qin, Z. L.; Zhao, J.; Zhao, S. L.; Xu, Z.; Taylor, A. D. An additive dripping technique using diphenyl ether for tuning perovskite crystallization for high-efficiency solar cells. *Nano Res.* **2018**, *11*, 2648–2657.

[8] Wu, W. Q.; Rudd, P. N.; Wang, Q.; Yang, Z. B.; Huang, J. S. Blading phase-pure formamidinium-alloyed perovskites for high-efficiency solar cells with low photovoltage deficit and improved stability. *Adv. Mater.* **2020**, *32*, 2000995.

[9] Fang, H. H.; Wang, F.; Adjokatse, S.; Zhao, N.; Even J.; Loi, M. A. Photoexcitation dynamics in solution-processed formamidinium lead iodide perovskite thin films for solar cell applications. *Light Sci. Appl.* **2016**, *5*, e16056.

[10] Yang, S.; Yao, J. C.; Quan, Y. N.; Hu, M. Y.; Su, R.; Gao, M.; Han, D. L.; Yang, J. H. Monitoring the charge-transfer process in a Nd-doped semiconductor based on photoluminescence and SERS technology. *Light Sci. Appl.* **2020**, *9*, 117.

[11] Wang, Q.; Chen, B.; Liu, Y.; Deng, Y. H.; Bai, Y.; Dong, Q. F.; Huang, J. S. Scaling behavior of moisture-induced grain degradation in polycrystalline hybrid perovskite thin films. *Energy Environ. Sci.* **2017**, *10*, 516–522.

[12] Shao, Y. C.; Fang, Y. J.; Li, T.; Wang, Q.; Dong, Q. F.; Deng, Y. H.; Yuan, Y. B.; Wei, H. T.; Wang, M. Y.; Gruverman, A. et al. Grain boundary dominated ion migration in polycrystalline organic–inorganic halide perovskite films. *Energy Environ. Sci.* **2016**, *9*, 1752–1759.

[13] Xu, X.; Li, K.; Yang, Z. Z.; Shi, J. J.; Li, D. M.; Gu, L.; Wu, Z. J.;

Meng, Q. B. Methylammonium cation deficient surface for enhanced binding stability at TiO$_2$/CH$_3$NH$_3$PbI$_3$ interface. *Nano Res.* **2017**, *10*, 483–490.

[14] Liu, L.; Huang, S.; Lu, Y.; Liu, P. F.; Zhao, Y. Z.; Shi, C. B.; Zhang, S. Y.; Wu, J. F.; Zhong, H. Z.; Sui, M. L. et al. Grain-boundary "patches" by *in situ* conversion to enhance perovskite solar cells stability. *Adv. Mater.* **2018**, *30*, 1800544.

[15] Niu, T. Q.; Lu, J.; Munir, R.; Li, J. B.; Barrit, D.; Zhang, X.; Hu, H. L.; Yang, Z.; Amassian, A.; Zhao, K. et al. Stable high-performance perovskite solar cells via grain boundary passivation. *Adv. Mater.* **2018**, *30*, 1706576.

[16] Saliba, M.; Matsui, T.; Seo, J. Y.; Domanski, K.; Correa-Baena, J. P.; Nazeeruddin, M. K.; Zakeeruddin, S. M.; Tress, W.; Abate, A.; Hagfeldt, A. et al. Cesium-containing triple cation perovskite solar cells: Improved stability, reproducibility and high efficiency. *Energy Environ. Sci.* **2016**, *9*, 1989–1997.

[17] Bu, T. L.; Liu, X. P.; Zhou, Y.; Yi, J. P.; Huang, X.; Luo, L.; Xiao, J. Y.; Ku, Z. L.; Peng, Y.; Huang, F. Z. et al. A novel quadruple-cation absorber for universal hysteresis elimination for high efficiency and stable perovskite solar cells. *Energy Environ. Sci.* **2017**, *10*, 2509–2515.

[18] Cho, K. T.; Paek, S.; Grancini, G.; Roldán-Carmona, C.; Gao, P.; Lee, Y.; Nazeeruddin, M. K. Highly efficient perovskite solar cells with a compositionally engineered perovskite/hole transporting material interface. *Energy Environ. Sci.* **2017**, *10*, 621–627.

[19] Jeon, N. J.; Noh, J. H.; Kim, Y. C.; Yang, W. S.; Ryu, S.; Seok, S. I. Solvent engineering for high-performance inorganic-organic hybrid perovskite solar cells. *Nat. Mater.* **2014**, *13*, 897–903.

[20] Xu, J. X.; Buin, A.; Ip, A. H.; Li, W.; Voznyy, O.; Comin, R.; Yuan, M. J; Jeon, S.; Ning, Z. J.; McDowell, J. J. et al. Perovskite-fullerene hybrid materials suppress hysteresis in planar diodes. *Nat. Commun.* **2015**, *6*, 7081.

[21] Bi, D. Q.; Gao, P.; Scopelliti, R.; Oveisi, E.; Luo, J. S.; Grätzel, M.; Hagfeldt, A.; Nazeeruddin, M. K. High-performance perovskite solar cells with enhanced environmental stability based on amphiphile-modified CH$_3$NH$_3$PbI$_3$. *Adv. Mater.* **2016**, *28*, 2910–2915.

[22] Wu, Y. Z.; Yang, X. D.; Chen, W.; Yue, Y. F.; Cai, M. L.; Xie, F. X.; Bi, E. B.; Islam, A.; Han, L. Y. Perovskite solar cells with 18.21% efficiency and area over 1 cm^2 fabricated by heterojunction engineering. *Nat. Energy* **2016**, *1*, 16148.

[23] Zheng, X. P.; Chen, B. C.; Dai, J.; Fang, Y. J.; Bai, Y.; Lin, Y.; Wei, H. T.; Zeng, X. C.; Huang J. S. Defect passivation in hybrid perovskite solar cells using quaternary ammonium halide anions and cations. *Nat. Energy* **2017**, *2*, 17102.

[24] Tan, F.; Tan, H.; Saidaminov, M. I.; Wei, M. Y.; Liu, M. X.; Mei, A.; Li, P. C.; Zhang, B. W.; Tan, C. S.; Gong, X. W. et al. *In situ* back-contact passivation improves photovoltage and fill factor in perovskite solar cells. *Adv. Mater.* **2019**, *31*, e1807435.

[25] Peng, J.; Wu, Y. L.; Ye, W.; Jacobs, D. A.; Shen, H. P.; Fu, X.; Wan, Y. M.; Duong, T.; Wu, N. D.; Barugkin, C. et al. Interface passivation using ultrathin polymer–fullerene films for high-efficiency perovskite solar cells with negligible hysteresis. *Energy Environ. Sci.* **2017**, *10*, 1792–1800.

[26] Mahmud, M. A.; Duong, T.; Yin, Y. T.; Peng, J.; Wu, Y. L.; Lu, T.; Pham, H. T.; Shen, H. P.; Walter, D.; Nguyen, H. T. et al. *In situ* formation of mixed-dimensional surface passivation layers in perovskite solar cells with dual-isomer alkylammonium cations. *Small* **2020**, *16*, 2005022.

[27] Jiang, Q.; Zhao, Y.; Zhang, X. W.; Yang, X. L; Chen, Y.; Chu, Z. M.; Ye, Q. F.; Li, X. X.; Yin, Z. G.; You, J. B. Surface passivation of perovskite film for efficient solar cells. *Nat. Photonics* **2019**, *13*, 460–466.

[28] Dingemans, G.; Terlinden, N. M.; Pierreux, D.; Profijt, H. B.; van de Sanden, M. C. M.; Kessels, W. M. M. Influence of the oxidant on the chemical and field-effect passivation of Si by ALD Al$_2$O$_3$. *Electrochem. Solid-State Lett.* **2011**, *14*, H1.

[29] Wang, F. Y.; Zhang, Y. H.; Yang, M. F.; Han, D. L.; Yang, L. L.; Fan, L.; Sui, Y. R.; Sun, Y. F.; Liu, X. Y.; Meng, X. W. et al. Interface dipole induced field-effect passivation for achieving 21.7% efficiency and stable perovskite solar cells. *Adv. Funct. Mater.*, in press, DOI: 10.1002/adfm.202008052.

[30] Yi, H. T.; Rangan, S.; Tang, B. X.; Frisbie, C. D.; Bartynski, R. A.; Gartstein, Y. N.; Podzorov, V. Electric-field effect on photoluminescence of lead-halide perovskites. *Mater. Today* **2019**, *28*, 31–39.

[31] Hwang, J. M. Plasma charge injection technology and its application to c-Si solar cells for field-effect passivation. *J. Appl. Phys.* **2019**, *125*, 173301.

[32] Glunz, S. W.; Biro, D.; Rein, S.; Warta, W. Field-effect passivation of the SiO₂Si interface. *J. Appl. Phys.* **1999**, *86*, 683–691.

[33] Yu, P. C.; Tsai, C. Y.; Chang, J. K.; Lai, C. C.; Chen, P. H.; Lai Y. C.; Tsai P. T.; Li, M. C.; Pan, H. T.; Huang, Y. Y. et al. 13% efficiency hybrid organic/silicon-nanowire heterojunction solar cell via interface engineering. *ACS Nano* **2013**, *7*, 10780–10787.

[34] Kong, W. G; Li, W.; Liu, C. W.; Liu, H.; Miao, J.; Wang, W. J.; Chen, S.; Hu, M. M.; Li, D. D.; Amini, A. et al. Organic monomolecular layers enable energy-level matching for efficient hole transporting layer free inverted perovskite solar cells. *ACS Nano* **2019**, *13*, 1625–1634.

[35] Yang, L. Y.; Cai, F. L.; Yan, Y.; Li, J. H.; Liu, D.; Pearson, A. J.; Wang, T. Conjugated small molecule for efficient hole transport in high-performance p-i-n type perovskite solar cells. *Adv. Funct. Mater.* **2017**, *27*, 1702613.

[36] Kalinowski, J.; Giro, G.; Cocchi, M.; Fattori, V.; Marco, P. D. Unusual disparity in electroluminescence and photoluminescence spectra of vacuum-evaporated films of 1,1-bis((di-4-tolylamino)phenyl) cyclohexane. *Appl. Phys. Lett.* **2000**, *76*, 2352–2354.

[37] Heymans, N. FTIR investigation of structural modification of polycarbonate during thermodynamical treatments. *Polymer* **1997**, *38*, 3435–3440.

[38] Khan, F.; Khanna, S.; Hor, A. M.; Sundararajan, P. R. Sundararajan, P. R. The role of molecular volume and the shape of the hole transport molecule in the morphology of model charge transport composites. *Can. J. Chem.* **2010**, *88*, 247–259.

[39] Jin, S.; Wei, Y. L.; Huang, F. Y.; Yang, X. M.; Luo, D.; Fang, Y.; Zhao, Y. Z.; Guo, Q. Y.; Huang, Y. F.; Wu, J. H. Enhancing the perovskite solar cell performance by the treatment with mixed anti-solvent. *J. Power Sources* **2018**, *404*, 64–72.

[40] Wang, F. Y.; Yang, M. F.; Zhang, Y. H.; Yang, L. L.; Fan, L.; Lv, S. Q.; Liu, X. Y.; Han, D. L.; Yang, J. H. Activating old materials with new architecture: Boosting performance of perovskite solar cells with H₂O-assisted hierarchical electron transporting layers. *Adv. Sci.* **2019**, *6*, 1801170.

[41] Li, X. Q.; Li, W. H.; Yang, Y. J.; Lai, X.; Su, Q.; Wu, D.; Li, G. Q.; Wang, K.; Chen, S. M.; Sun, X. W. et al. Defects passivation with dithienobenzodithiophene based π-conjugated polymer for enhanced performance of perovskite solar cells. *Sol. RRL* **2019**, *3*, 1900029.

[42] Zhang, C. C.; Li, M.; Wang, Z. K.; Jiang, Y. R.; Liu, H. R.; Yang, Y. G.; Gao, X. Y.; Ma, H. Passivated perovskite crystallization and stability in organic-inorganic halide solar cells by doping a donor polymer. *J. Mater. Chem. A* **2017**, *5*, 2572–2579.

[43] Privitera, A.; Righetto, M.; De Bastiani, M.; Carraro, F.; Rancan, M.; Armelao, L.; Granozzi, G.; Bozio, R.; Franco, L. Hybrid organic/inorganic perovskite-polymer nanocomposites: Toward the enhancement of structural and electrical properties. *J. Phys. Chem. Lett.* **2017**, *8*, 5981–5986.

[44] Wu, Y. Q.; Wang, P.; Zhu, X. L.; Zhang, Q. Q.; Wang, Z. Y.; Liu, Y. Y.; Zou, G. Z.; Dai, Y.; Whangbo, M. H.; Huang, B. B. Composite of CH₃NH₃PbI₃ with reduced graphene oxide as a highly efficient and stable visible-light photocatalyst for hydrogen evolution in aqueous HI solution. *Adv. Mater.* **2018**, *30*, 1704342.

[45] Wang, F. Y.; Zhang, Y. H.; Yang, M. F.; Yang, L. L.; Sui, Y. R.; Yang, J. H.; Zhao, Y.; Zhang, X. D. Realization of 16.9% efficiency on nanowires heterojunction solar cells with dopant-free contact for bifacial polarities. *Adv. Funct. Mater.* **2018**, *28*, 1805001.

[46] Wang, F. Y.; Zhang, Y. H.; Yang, M. F.; Du, J. Y.; Xue, L. L.; Yang, L. L.; Fan, L.; Sui, Y. R.; Yang, J. H.; Zhang, X. D. Exploring low-temperature processed a-WO_x/SnO₂ hybrid electron transporting layer for perovskite solar cells with efficiency >20.5%. *Nano Energy* **2019**, *63*, 103825.

[47] Staub, F.; Hempel, H.; Hebig, J. C.; Mock, J.; Paetzold, U. W.; Rau, U.; Unold, T.; Kirchartz, T. Beyond bulk lifetimes: Insights into lead halide perovskite films from time-resolved photoluminescence. *Phys. Rev. Appl.* **2016**, *6*, 044017.

[48] He, Z. C.; Zhong, C. M.; Huang, X.; Wong, W. Y.; Wu, H. B.; Chen, L. W.; Su, S. J.; Cao, Y. Simultaneous enhancement of open-circuit voltage, short-circuit current density, and fill factor in polymer solar cells. *Adv. Mater.* **2011**, *23*, 4636–4643.

[49] Tan, W. Y.; Wang, R.; Li, M.; Liu, G.; Chen, P.; Li, X. C.; Lu, S. M.; Zhu, H. L.; Peng, Q. M.; Zhu, X. H. et al. Lending triarylphosphine oxide to phenanthroline: A facile approach to high-performance organic small-molecule cathode interfacial material for organic photovoltaics utilizing air-stable cathodes. *Adv. Funct. Mater.* **2014**, *24*, 6540–6547.

[50] Xie, J. S.; Huang, K.; Yu, X. G.; Yang, Z. R.; Xiao, K.; Qiang, Y. P.; Zhu, X. D.; Xu, L. B.; Wang, P.; Cui, C. et al. Enhanced electronic properties of SnO₂ via electron transfer from graphene quantum dots for efficient perovskite solar cells. *ACS Nano* **2017**, *11*, 9176–9182.

[51] Pockett, A.; Eperon, G. E.; Peltola, T.; Snaith, H. J.; Walker, A.; Peter, L. M.; Cameron, P. J. Characterization of planar lead halide perovskite solar cells by impedance spectroscopy, open-circuit photovoltage decay, and intensity-modulated photovoltage/photocurrent spectroscopy. *J. Phys. Chem. C* **2015**, *119*, 3456–3465.

[52] Bai, Y.; Dong, Q. F.; Shao, Y. C.; Deng, Y. H.; Wang, Q.; Shen, L.; Wang, D.; Wei, W.; Huang, J. S. Enhancing stability and efficiency of perovskite solar cells with crosslinkable silane-functionalized and doped fullerene. *Nat. Commun.* **2016**, *7*, 12806.

[53] Cho, Y.; Soufiani, A. M.; Yun, J. S.; Kim, J.; Lee, D. S.; Seidel, J.; Deng, X. F.; Green, M. A.; Huang, S. J.; Ho-Baillie, A. W. Y. Mixed 3D-2D passivation treatment for mixed-cation lead mixed-halide perovskite solar cells for higher efficiency and better stability. *Adv. Energy Mater.* **2018**, *8*, 1703392.

[54] Liu, K. K.; Liu, Q.; Yang, D. W.; Liang, Y. C.; Sui, L. Z.; Wei, J. Y.; Xue, G. W.; Zhao, W. B.; Wu, X. Y.; Dong, L. et al. Water-induced MAPbBr₃@PbBr(OH) with enhanced luminescence and stability. *Light Sci. Appl.* **2020**, *9*, 44.

[55] Zhou, H. P.; Chen, Q.; Li, G.; Luo, S.; Song, T. b.; Duan, H. S.; Hong, Z.; You, J. B.; Liu, Y. S.; Yang, Y. Interface engineering of highly efficient perovskite solar cells. *Science* **2014**, *345*, 542–546.